Effect of aerosol concentration on post-corona unipolar diffusion charging: ion density retro-controlled by aerosol space charge versus geometry of ion-aerosol mixing

N Jidenko, A Bouarouri, J.-P. Borra

Effect of aerosol concentration on post-corona unipolar diffusion charging: ion density retro-controlled by aerosol space charge versus geometry of ion-aerosol mixing

N. Jidenko, A. Bouarouri & J.-P. Borra

Université Paris-Saclay, CNRS, Laboratoire de Physique des Gaz et des Plasmas, 91405, Orsay, France.

Abstract: The influence of aerosol concentration on the charge per particle is investigated in post-DC corona diffusion chargers for particle diameter between 10 nm and 1 µm. Particles are charged as they pass through the charger volume by collection of ions; the ion concentration decreases along the same path due to unipolar space charge repulsion and collection on walls. With crossflow of ions and aerosols, the final mean charge per particle decreases by up to one order of magnitude with increasing aerosol concentration from 10^9 to 10^{11} m^{-3}. The evolution of the ion density profile along particle trajectories with aerosol concentration is shown to be due to the consumption of ions by aerosol charging and to ion dispersion by unipolar space charge repulsion including ions and charged particles. Both are investigated using a simplified 1.5D model with axial symmetry and homogeneous mixing of ions and aerosols. It is shown that, for a given operating condition, the aerosol space charge is responsible for the modification of the spatial ion distribution and the related lower $N_i \times \tau$ and charge per particle reported at higher aerosol concentration. From calculations, we define the maximal aerosol concentration to keep the mean charge per particle unaffected by aerosol space charge in the optimal case of homogeneous mixing of ion and aerosol. Finally, the comparison of different ion-aerosol mixing conditions highlights that an axial symmetry of the charger reduces the influence of aerosol space charge. This effect of aerosol concentration on the particle charge is critical for aerosol chargers devoted to electric mobility selection for size measurements or focused electro-deposition, as well as for concentration measurements as performed using emerging low cost sensors based on corona chargers.

Keywords: corona discharge, diffusion charging, ion losses, space charge, electrostatic repulsions

1 Introduction

Due to the low cost, simplicity and reliability, electrical discharges at atmospheric pressure are commonly used to produce high densities of unipolar ions for aerosol charging (Borra 2006; Intra and Tippayawong 2011; Whitby 1961; Zheng et al. 2016). When aerosols are injected into the discharge gap, two charging mechanisms are involved. Diffusion charging is active for all particle sizes contrary to the field charging that mainly concerns particles larger than 100 nm (Liu and Kapadia 1978). Most aerosol chargers operate in post-discharge, meaning that two separate gas flows, one containing aerosol and the other containing ions, are mixed downstream of the ion source, which is typically an electric discharge. This is done to limit aerosol losses in the discharge gap and the subsequent discharge destabilization, as well as the ions mobility dependence on gas composition of the sampled aerosol. In this operating mode, without Laplace electric field (due to polarized electrodes), particles are charged only by ion diffusion.

Diffusion charging is well documented with experimental results (Adachi et al. 1987; Alonso, Martin and Alguacil 2006; Biskos, Reavell and Collings 2005; Borra, Jidenko and Bourgeois 2009; Chen, Jiang and Chen 2019; Choi and Kim 2007; Domat, Kruis and Fernandez-Diaz 2014b; Hewitt 1957; Laitinen and Keskinen 2016; Medved et al. 2000; Park, An and Hwang 2007; Pui, Fruin and McMurry 1988; Qi and Kulkarni 2012; Unger and Borra 2000; Vivas, Hontañón and Schmidt-Ott 2008; Whitby 1961), numerical models (Alonso, Alguacil and Borra 2009; Biskos, Mastorakos and Collings 2004; Domat, Kruis and Fernandez-Diaz 2014a; Nishida et al. 2019) and theoretical approaches (Bricard 1949; Fuchs 1963; Marlow and Brock 1975; Veshchunov 2021; White 1951). Diffusion charging follows a stochastic mechanism leading to charge distributions of particles of a given diameter. The mean charge per particle depends on aerosol diameter and shape, $N_i \times \tau$ product (with τ, in s, the transit time of particle in any given ion density N_i, in m^{-3}) and ion properties (mass and electrical mobility). The standard deviation of charge distribution depends on particle diameter, gas temperature and the different $N_i \times \tau$ product crossed by particles along different trajectories.

Different laws describe the evolution of the mean charge per particle with time in homogeneous local unipolar ion density. One of the main assumptions of these laws is the steady flux of ions towards particle (i.e. a steady state with negligible evolution of ion density far from particle surface i.e. out of the collection volume within which ions collide with the particle). Fuchs has demonstrated that this steady state approximation is valid as long as $N_i < 5 \cdot 10^{-6} \times d_p^{-3}$ (e.g. for 100 nm particle, the ion density should not exceed 5×10^{15} m^{-3}) (Fuchs 1963). This condition on maximal ion density is fulfilled in most aerosol chargers due to the decay of unipolar ion density by self-repulsion and is used in this paper for calculations. The main concern of this paper is the evolution of the ion density profile with aerosol concentration.

For aerosol electro-processing and measurement tools, an "ideal" aerosol charger, in particular for nanoparticles, should reach maximum mean charge per particle with minimal impact on the aerosol size distribution (Flagan 1998). Therefore, post-discharge diffusion chargers generally operate with a short aerosol transit time at an initial ion density, usually above 10^{14} m^{-3} (Intra and Tippayawong 2011). In these conditions, the electric field generated by the ion space charge leads to ion losses to the walls and thus to a decay in the ion density (below 10^{13} m^{-3} in a few tens of ms) along the charging volume (Whitby 1961). The consequences of decreasing ion density on aerosol charging i.e. the evolution of the number of ions per particle with aerosol concentration has already been investigated for bipolar charging (Alonso and Alguacil 2003; de La Verpilliere, Swanson and Boies 2015; Hoppel and Frick 1988; Tigges, Jain and Schmid 2015). For unipolar charging, the evolution of the number of ions per particle with aerosol concentration affects the $N_i \times \tau$ integrated along particle trajectory but no significant effect are reported in chargers with axial symmetry (Alonso, Alguacil and Borra 2009; Domat, Kruis and Fernandez-Diaz 2014a). The final mean charge per particle depends on the ion density profile along its trajectory. The spatial distribution of ion density and particle trajectory define the charging conditions (Huang and Alonso 2012). The particle trajectory depends on the injection position in the ionic cloud, as well as on electrical and drag forces. Moreover, particle trajectory and ion density are coupled as particle trajectory depends on the charging dynamics and ion density depends on the space charge electric field including charged aerosol (Unger 2001).

To limit these drawbacks (i.e. to reduce ion density heterogeneities in the charging volume), ion injection along the charging volume (Biskos, Reavell and Collings 2005; Hewitt 1957) or turbulent mixing of aerosol and ion (Medved et al. 2000) have been successfully tested. Other simple, cheap and reliable post-corona diffusion chargers with a single ion injection can lead to initial ion density over 10^{15} m^{-3}, targeted for specific applications like nanoparticle charging with limited particle losses for charging time shorter than 50 ms (Alonso and Huang 2015; Borra, Jidenko and Alonso 2012; Domat, Kruis and Fernandez-Diaz 2014a; Intra, Yawootti and Rattanadecho 2017). However, for particle size or concentration measurements of polydisperse aerosol, the size-charge relation should be independent of the aerosol concentration to calculate the concentration from charged aerosol current or to limit ambiguities in data inversion from mobility spectra to aerosol size distribution. This implies that the current of charged particles of a given size has to be linear with the aerosol concentration. Otherwise, the influence of the total aerosol concentration on the measurement has to be taken into account to estimate the concentration of aerosol for each size range using approximations such as starting calculations with an expected size distribution to calculate the real one by a trial and error method.

Previous studies with crossflow mixing of ion and aerosol jets have shown that particles should be injected as close as possible to the ion injection to reach a high mean charge per particle that can decrease by a factor 10 for aerosol concentration from 10^{9} to 10^{13} m^{-3} (Bouarouri 2014; Unger and Borra 2000). Three effects can explain the reduction of ion density and the related mean charge per particle measured downstream of the charger with increasing aerosol concentration. The aerosol space charge can limit the ion flux injected in the post-

corona charging volume. Besides, the consumption of ions for aerosol charging reduces the supply of free ions available for aerosol charging. In other words, the reduction of the number of ions per particle with aerosol concentration could affect the $N_i \times \tau$ integrated along particle trajectory. The third effect is the electrostatic repulsions between ions and the space charge including ions and less mobile charged aerosols.

This paper addresses the influence of aerosol concentration on the mean charge per particle measured downstream in post-corona chargers with a single ion injection and the three effects described above. Data are first presented for a charger with a crossflow mixing of ion and aerosol designed to use particle inertia to reach a constant size-charge relation above 200 nm (Jidenko et al. 2020). The results are then compared with those obtained in various arrangements. A simple model with axial symmetry is used to investigate each of the three effects independently. In the last section, based on these calculations, we define a condition to limit the influence of aerosol concentration on the mean charge per particle.

2 Experimental setup and methods

The experimental set-up, depicted in Fig. 1, can be divided in three parts: aerosol production, corona charger (including ion production by the corona discharge and aerosol charging in post-discharge) and charged aerosol characterization.

Pressurized air passes through a dryer (relative humidity below 0.3 %), a high efficiency particle filter (no particle detected above 2.5 nm) and a gas purifier (volatile organic compound concentration below 6 ppmv). Three flow controllers regulate the aerosol generator flow rate (Q_p), the dilution factor $F = (Q_i+Q_p)/Q_p$ and the discharge flow rate (Q_i) used to extract the ions from the discharge gap toward the post-discharge charging volume.

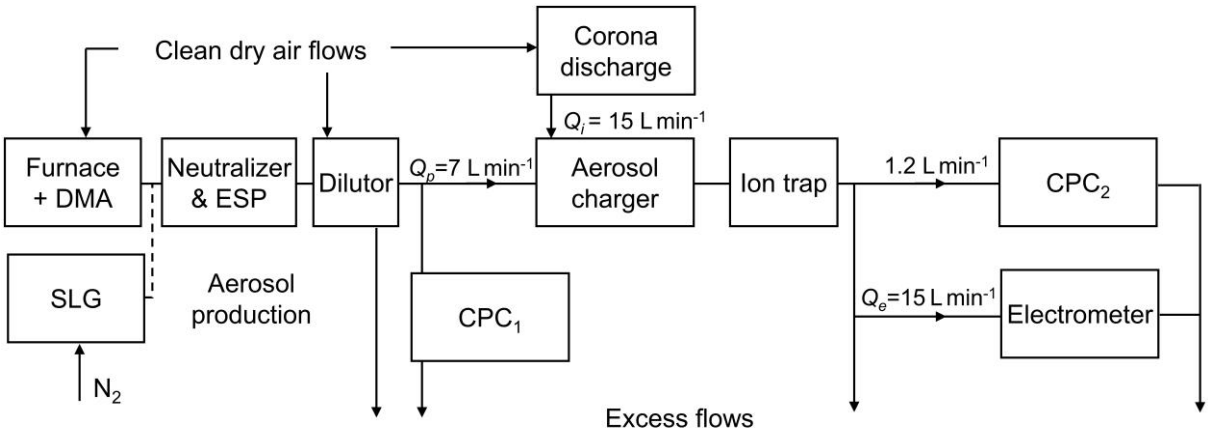

Fig. 1. Flow diagram of the experimental setup (CPC: condensation particle counter, ESP electrostatic precipitator, SLG Sinclair Lamer generator, DMA differential mobility analyzer)

Both pressures in the discharge volume and the aerosol charger are measured. The average transit time of aerosol in the charging volume is set at 50 ms to limit aerosol losses. The charger geometry has been adapted to gas flow rates for a mean transit time of 50 ms.

2.1 Monodisperse aerosol production

To accurately measure the number of charges per particle, one has to produce a monodispersed aerosol with controlled mean diameter, d_p, flow rate Q_p, initial mean charge per particle and concentration N_p. Two different generators were used to generate aerosol from 10 nm to 1 µm.

A Sinclair Lamer Generator (SLG) produces droplets of Di-Ethyl-Hexyl Sebacate (DEHS) by nebulization of a solution of sodium chloride (NaCl), followed by heterogeneous condensation of DEHS on the dry NaCl residues.

A furnace produces NaCl particles neutralized by a ^{85}Kr source and classified in a long-column DMA. The DMA was operated with aerosol and sampling flow rates of 2 L min^{-1}, for sheath and excess flow rates of 20 L min^{-1}. To avoid particle sizing errors due to multi-charged particles, the mobility selection was performed for particle size larger than the modal diameter (Alonso, Gomez and Borra 2014). The modal diameter of the so-produced aerosol is controlled by the temperature of the furnace and the aerosol transit time to the DMA at constant gas flow rate of 2 L min^{-1}. Then, the voltage applied to the DMA controls the final modal diameter.

To generate uncharged particles of controlled size, the so-produced monodispersed particles were then passed successively through a ^{85}Kr neutralizer (74 MBq) and an electrostatic precipitator (ESP) to remove all charged particles. The main characteristics of these generators are summarized in Table 1.

Table 1. Main characteristics of the monodisperse aerosol generators; values correspond to the available ranges

Generator	Principle	*modal* d_p (nm)	Q_p (L min^{-1})	N_p (m^{-3}) before neutralization	$N_p{}^n$ (m^{-3}) after neutralization	σ_g
SLG	Heterogeneous condensation	350-1000	4.3	$3\cdot10^{12}$	$3\text{-}6\cdot10^{11}$	1.2
Furnace + DMA	Homogeneous nucleation and mobility selection	10-300	2	$2\text{-}10\cdot10^{10}$	$0.4\text{-}2\cdot10^{10}$	<1.2

The aerosol concentration was then controlled with a dilution factor between 2 and 30 using a homemade dilutor; and between 85 and 150 with the Palas VLK100.
Size distributions have been checked before and after dilution for both generators. The geometric standard deviations of the size distributions are lower than 1.2, the aerosol can thus be considered as monodisperse.

2.2 Corona charger: discharge operating conditions and currents measurements

The corona charger is shown in Fig. 2. The corona discharge used here as an ion source is built in a cylindrical tube of polyacetal with two metal electrodes: a plane and a needle. A polyacetal piece hold the stainless steel needle, ended in a sharp tip covered by tungsten with a radius of curvature of 80 µm, perpendicular to the 1 mm thick, grounded metal plane. This grounded plate had a 2 mm diameter hole for ion injection. The needle is screwed into the central piece to control the gap length (d) between the tip and the grounded plane. The needle is connected through a 5 MΩ resistor (R) to a negative DC high voltage power supply (V). All the measurements have thus been carried out in Trichel or Corona regimes excluding the transition regime (cf. §S2.1 of supplemental information, SI).

Ions are drawn from the ionizer within a gas flow of Q_i = 15 L min^{-1} injected near the needle from a 3 mm inner diameter tube and then flow through a 2 mm hole drilled in the ground plane the axis of the needle. On the wall of the charging volume, the grounded plane is covered with a 500 µm thickness plane of Teflon (to limit the collection of ions, hereafter referred as insulator plane) with a 2 mm hole on the centre. The arrangement of the extraction hole is critical in terms of ion transfer from the discharge volume to the post-discharge volume as up to 90% of the ions can be collected on the plane and on the inner surface of the extraction hole (Bouarouri et al. 2016).

The charging volume is enclosed within a copper tube of 20 mm diameter, which was positioned with a 45° angle to the needle axis. The aerosol injector is a 2 mm diameter channel, perpendicular to the needle axis and shifted by 4 mm in both directions from the ion output as depicted in Fig. 2. The aerosol gas flow rate (Q_p = 7 L min^{-1}) leads to a mean aerosol injection velocity of 37 m s^{-1}. For a total gas flow rate of 22 L min^{-1}, the mean transit time in the charging volume is 50 ms. The aerosol concentrations presented here take into account the dilution factor (F = 22/7). The pressures are 1030 hPa and 960 hPa in the discharge gap and in the charger volume respectively.

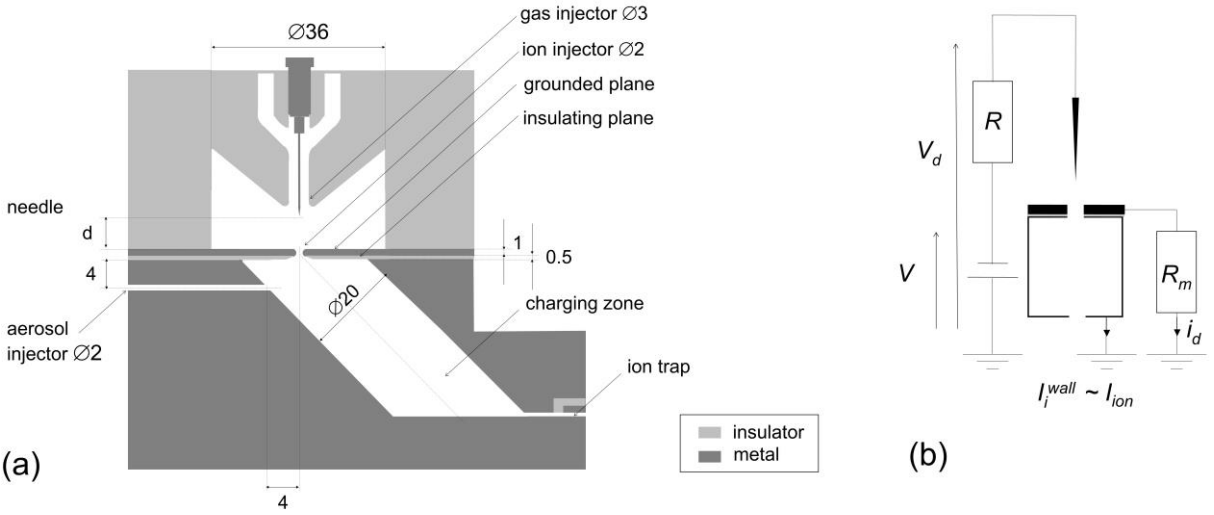

Fig. 2. (a) Post-diffusion charger geometry referred as perpendicular 1 (b) electrical measurement setup

The post-discharge ion current injected in the charging volume, I_{ion} is a critical parameter of the charger characterization to control the discharge regime and intensity. Special care has been taken for discharge characterization: measurements of voltage, mean discharge and ion currents were made in addition to the instantaneous discharge current (i_d) to define the discharge regime and the stability of the discharge. The discharge regime and the stability of the discharge affect the initial ion density at the entrance of the charging volume, N_i° and the ion-aerosol mixing. To fully characterize the discharge, we have measured:

- the applied voltage V_d with a high voltage probe (Tektronix P6015),
- the discharge current, $i_d(t)$ with an oscilloscope by measuring the voltage drop either on a 50 Ω (for Trichel characterization) or a 100 kΩ resistor, R_{mes} placed between the grounded plane and the ground,
- the mean discharge current I_d with a voltmeter with a response time of 0.3 s,
- the post-discharge ion currents: I_i^{wall} (collected on the metal wall of the charging volume) and I_i^{out} (collected by the ion trap downstream the charging volume) are both measured with a Keithley electrometer or an oscilloscope. I_i^{wall} can thus be considered as the ion flux blown by the gas flow in the charging volume ($I_{ion} = I_i^{wall} + I_i^{out}$) as I_i^{out} represents less than 1% of I_i^{wall}.

Neglecting eventual chemical surface reaction that may leads to ion production in the charger, the ion density at the entrance of the charging volume (i.e. at the outlet of the ion injector), $N_i^{injector}$ can be estimated from I_{ion} by :

$$N_i^{injector} = \frac{I_{ion}}{e \cdot S(v_g + Z_i \cdot E)} \quad (1)$$

with e is the elementary charge, S the section of the ion injector (12.6×10^{-6} m^2), v_g the mean gas velocity in the injector (79 m s^{-1} for Q_i=15 L min^{-1}), Z_i the mean electrical mobility of negative ions (1.8×10^{-4} m^2 V^{-1} s^{-1} estimated from previous measurement in a similar corona charger with

a high resolution mobilimeter) and E the electric field at the output of the injector (Bouarouri et al. 2016). In these conditions, the electric field at the entrance of the charging volume is about 10^5 V m^{-1}, the resulting ion electrical drift velocity ($Z_i \cdot E$) represents about 20% of the ion velocity resulting from flow and can be neglected, as a first approximation.

2.3 Charge measurements

The mean charge per particle is calculated from the particle concentration (N_p) measured with a Condensation Particle Counter (CPC, 3022, TSI) and the total aerosol current (I_e) measured with a Faraday cup electrometer (FCE, 3068A, TSI) by: $< q_p >= \frac{I_e}{Q_e \cdot N_p \cdot e}$ (2)

where Q_e is the flow rate in the FCE. This approximation leads to less than 12 % error mostly due to uncertainties on FCE and CPC gas flow rates) under the condition that:

- Aerosols are monodispersed (geometric standard deviation of the size distribution σ_g = 1.2). The mean charge per particle calculated this way can be attributed to the mean particle diameter.
- Ions are removed from the charged particle flow before the FCE (to avoid an overestimation of the mean charge). The difference between electrical mobilities of gaseous ions (~1.8×10^{-4} m^2 V^{-1} s^{-1}) and charged particles (10^{-9} – 10^{-7} m^2 V^{-1} s^{-1}) allows one to use an ion trap to precipitate the ions before sampling particle with particle losses below 2%.
- The offset of the FCE (few fA) is subtracted from the charged particle current.
- Aerosol losses during transport by diffusion and electrostatic self-repulsion are considered to be either negligible or the same in both the CPC and the FCE lines (they could possibly be quantified to control the particle concentration at the entrance of the FCE). For particles between 70 nm and 1 µm, less than 10% are lost during the 50 ms transit time in the charging chamber, measured as (N_p^1-F·N_p^2)/N_p^1 with N_p^1 and N_p^2 the aerosol concentrations measured by CPC_1 and CPC_2 respectively).
- The corona discharge does not produce particle. Electrical discharges can in fact produce fine nanoparticles by physical nucleation of vaporized electrode or by reactive nucleation of chemical by-products (Alonso, Martin and Alguacil 2006; Borra et al. 1998; Liu et al. 1987; Nolan and Kuffel 1957). The gas injected in the discharge should be dry and clean and in addition, filamentary discharges crossing the whole gap, such as streamer or spark must be avoided.

3 Results and discussion

3.1 Influence of aerosol concentration on the mean charge per particle

The reduction of the mean charge per particle with aerosol concentration is first reported in the charger with perpendicular crossflow mixing of ions and aerosols and then compared to the case of different ion-aerosol mixing conditions in order to highlight the effect of aerosol space charge.

3.1.1 Charger with perpendicular crossflow mixing of ions and aerosols

As expected from diffusion charging theories, it has first been confirmed that, for a given aerosol, the mean charge per particle increases with the mean $N_i \times \tau$ product, here controlled by the discharge current. For instance, the mean charge per 350 nm particles evolves from -3.8 to -6.3 elementary charge when the discharge current increases from -10 to -110 µA, for an aerosol concentration of 10^{10} m^{-3}. The negative mean charge per particle are hereafter presented in absolute values.

The ion source can be considered as constant in a given operating condition (constant pressure, temperature, applied voltage and gas flow rates) for all the different monodisperse aerosols tested here. The post-discharge ion currents (I_{ion}) measured with or without particle are the same up to $N_p = 10^{12}$ m^{-3}. Nevertheless, even if I_{ion} is constant, the ion density on each point of the charger depends on the monodisperse aerosol concentration, as shown below. In the worst case (not presented here), for polymodal oil droplets of 400 nm at 2×10^{14} m^{-3}, I_{ion} decreases by 3% with the injection of particles.

Fig. 3 represents the mean charge per particle as a function of outlet aerosol concentration (from CPC2). The discharge operating conditions are summarized in Table 2. For these two cases, aerosol losses are lower than 5 %. Below 10^{10} m^{-3}, the dilutor changes the mean particle diameter by less than 7%, which affects the decay of the mean charge (cf. 91 nm in Fig. 3b).

Table 2. Operating conditions

Particle size d_p (nm)	Range of particle concentration after dilution N_p (m^{-3})	Gap length, d (mm)	Needle voltage V_d (kV)	Discharge current I_d (µA)	I_i^{wall} (nA)
91	2.6×10^9 - 5×10^{10}	9	- 6.88	- 30	- 710
350	1.6×10^9 - 1.5×10^{11}	5	- 4.15	- 100	- 580

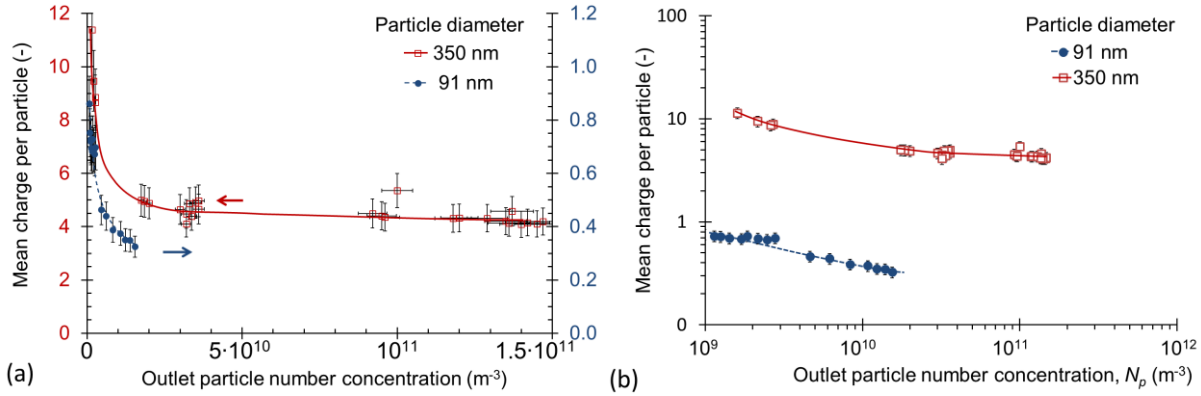

Fig. 3. Mean charge per particle for DEHS droplets of 350 nm and NaCl particle of 91 nm as a function of outlet aerosol concentration, with ion and aerosol gas flows of 15 and 7 L min^{-1} respectively and a mean transit time of 50 ms with (a) linear axis and (b) log axis.

As shown in Fig. 3, the final mean charge per particle q_p decreases from 11 to 4 elementary charges for 350 nm particle with aerosol concentration from 10^9 to 10^{11} m^{-3} and from 0.7 to 0.3 e for 91 nm particle from 2×10^9 to 5×10^{10} m^{-3}. The mean charge decreases for increasing concentration from 10^9 to 10^{10} m^{-3} whatever the nature of particles (DEHS, NaCl, polystyrene latex) and the discharge operating conditions. The same trends have already been reported with intensities depending on particle size and on post-corona charger ion-aerosol flows mixing arrangements (Bouarouri 2014; Jidenko et al. 2012; Unger 2001) (cf. §2.1 of SI).

The following reasons for the reduction of the mean charge per particle with increasing aerosol concentrations have first been excluded by preliminary tests:
- artefactual electrometer measurements, since the electrometer has been calibrated using a DMA and the offset, lower than a few fA, is subtracted from the measured particle current (cf. §2.3),
- reduction of ion mobilities due to condensation of volatile organic compounds, produced by the aerosol generator, on ions; since this effect has been observed with two generator types (furnace and SLG).

Therefore, the smaller charge per particle results from smaller ion density along the path of particles at higher aerosol concentration. The reduction of ion densities with aerosol concentration is investigated using experimental data and simple calculations. For the given 50 ms transit time, the $N_i \times t$ have been evaluated from data in Fig. 4 and Fuchs' theory from 2×10^{11} to 5×10^{11} and from 5×10^{11} to 6×10^{12} s m^{-3} for particles of 91 and 350 nm respectively.

The dispersion of ions is mainly controlled by the ion space charge as described by Whitby (Jayaratne et al. 2019; Whitby, Liu and Peterson 1965); nevertheless, aerosol space charge, surface electric field and Laplace electric field as well as the gas flow also affect the ion density in the charging volume. Moreover, the reduction of ion densities due to the consumption of ions by particle charging also accounts for the reduction of ion densities along the charger but can be neglected due to the large excess of ions compared to particles (as shown in §3.2). The flow profile can be considered as constant whatever the aerosol concentration tested here, since particles increase the linear momentum of the aerosol by less than 0.1% (the maximal mass concentration of particles of 10^{-3} kg.m^{-3} is much lower than the air density of 1.2 kg.m^{-3}).

The modification of the surface electric field related to the collection of ions on the insulating plane around the ion injector in the charger is negligible as the polarization is constant for a given operating condition (cf. §4.2 of the SI).

The number of ions injected into the charging volume per time unit can be considered as constant. In fact, the expected reduction of post-discharge ion current due to aerosol space charge field is not measurable for aerosols with concentration lower than 10^{12} m^{-3}.

Three experimental results tend to support the idea that despite the fact that aerosol space charge is much lower than ion space charge, aerosol space charge mainly accounts for the reduction of the charge with increasing aerosol concentration.

The ion flux from the corona discharge gap is reduced by the injection of high concentration of aerosol (above 10^{13} m^{-3}). The aerosol space charge electric field therefore limits the injection of ions in the charger from the corona discharge gap. This demonstrates that aerosol space charge can modify the ion density.

In addition, the reduction of $N_i \times \tau$ with aerosol concentration is larger for bigger 350 nm particles acquiring more charges and thus leading to higher space charge than for 91 nm particles.

At last, the geometry of ion-aerosol mixing is critical; the influence of aerosol space charge is reduced in chargers with axial symmetry as detailed in the following section.

3.1.2 Role of the symmetry of the ion-aerosol mixing

The effect of aerosol concentration on the mean charge per particle has been investigated in 6 chargers described in Fig. 4. Data are presented for mixings with and without axial symmetry in Fig. 4 (a) and (b) respectively. Axisymmetric flow mixing is achieved with a symmetry of both the electric field and the gas flow velocity. The descriptions of the aerosol chargers are given in the legend of Fig. 4.

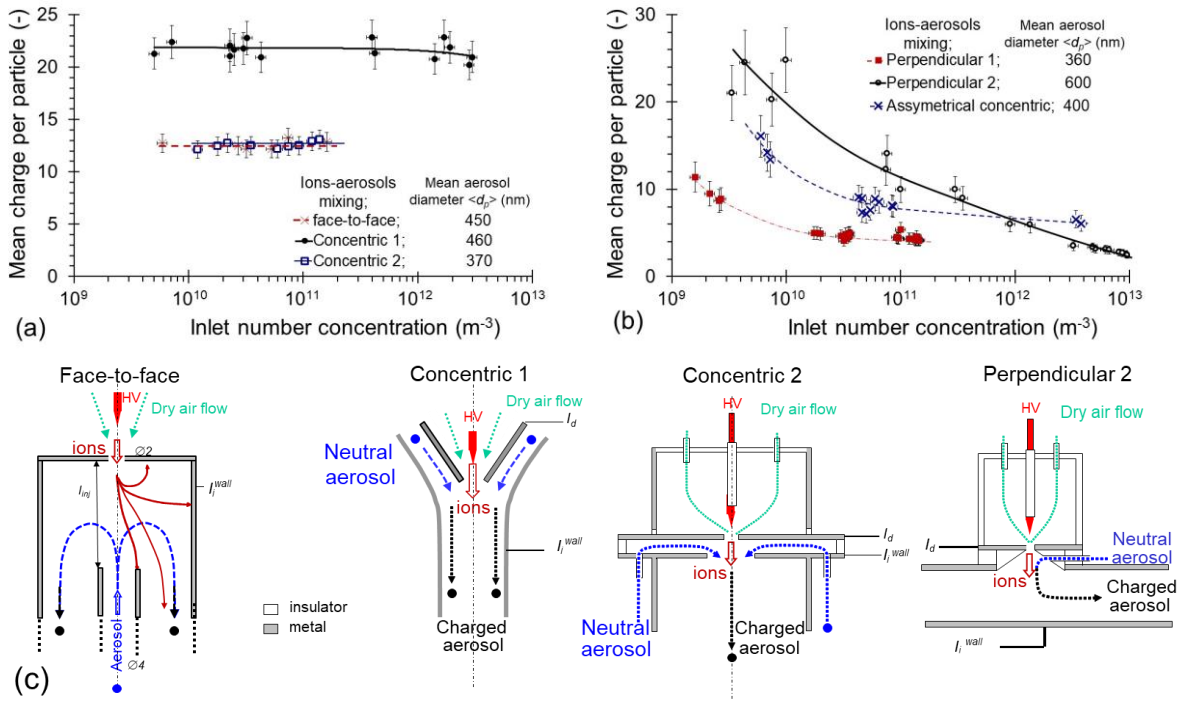

Fig. 4. Mean charge per particle as a function of aerosol concentration for various ion-aerosol mixing conditions (a) with axial symmetry: Face-to-face, aerosol in injected in front of the ion flux (V_d = -12 kV I_d = -30 µA, I_{ion} = -265 nA, Q_i=Q_a=30 L min^{-1}); Concentric 1, with co-flow mixing (V_d = -16.5 kV I_d = -110 µA, I_{ion} = -45 nA Q_i=Q_a=2 L min^{-1}) and concentric 2 with perpendicular mixing (V_d = -12 kV I_d = -30 µA, I_{ion} = -370 nA Q_i=Q_a=30 L min^{-1}) and (b) without axial symmetry: perpendicular 1, see section 3.1.1; perpendicular 2, with aerosol injected closer to the ion flux (V_d = .8 kV, I_d = 6 µA Q_i= 3 L min^{-1} Q_a = 6.6 L min^{-1}); asymmetrical concentric, concentric 1 with the discharge point 2 mm away from the axis of symmetry (V_d = -2.05 kV, I_d = -6 µA, I_{ion} =-45 nA, Q_i = Q_a = 2 L min^{-1})

To summarize these results, in the three ion-aerosol mixing conditions with axial symmetries (two concentric and a face-to-face mixings cf. Fig. 4 (a)), the measured mean charge per particle is constant up to an aerosol concentration of at least 10^{11} m^{-3}.

For the chargers without axial symmetry (only planar symmetry of the mixing), the mean charge per particle decreases with aerosol concentration from the lowest concentration of a few 10^9 m^{-3}. In these geometries, the aerosol space charge repels ions toward the walls and away from the aerosol flow; this reduces the $N_i \times t$ product even more as the aerosol concentration increases, such that ion density is retro-controlled by aerosol space charge.

3.2 Numerical calculations in axial geometry with homogeneous mixing

To investigate the influence of aerosol concentration on ion density profiles and subsequent $N_i \times \tau$ values, a 1.5D model with axial symmetry has been used:

- to quantify the influence of ion consumption for aerosol charging on the final mean charge per particle,
- to show that aerosol space charge alters the final mean charge per particle even in chargers with axial symmetry,
- and to define a condition on the maximum aerosol concentration (N_p^{max}) so that ion consumption by aerosol has a negligible effect on the final charge of particles (cf. §3.2.3).

3.2.1 Assumptions and methods

The model takes into account the reduction of ion density due to the space charge assuming plug flow as well as constant radial ion density and aerosol concentration in a tubular axisymmetric post-corona charger volume (i.e. an homogeneous mixing of ions and aerosols) with no particle losses and no Laplace nor surface electric field (cf. §4 of SI).

Due to these rough approximations (detailed in §4 of SI: real ion density profile, ion mobility evolution, surface electric and Laplace electric fields, particle inertia…), the results of the model cannot account quantitatively for all the experimental results. Nevertheless, the semi-quantitative results of the model are used to analyze the trends of the experimental data.

The input ranges of initial conditions injected in the model (N_i^0, N_p and d_p) are related to experimental conditions and lead to mean charge that agrees with experimental results within 30 %, for particles smaller than 200 nm (with Stokes number smaller than 0.02, i.e. for particles with negligible inertia). The properties of ions used in the model are: electrical mobility $Z_i = 1.8$ m^2 s^{-1} V^{-1} (mean mobility of ion measured by a high resolution mobility spectrometer) and mass of 80 atomic mass unit (classical value referred in the literature for negative ion (Reischl et al. 1996)). The pressure is fixed at 10^5 Pa and the temperature at 293 K.

Three ion densities are defined: $N_i^{injector}$ is the ion density at the entrance of the charging volume, N_i^m is the maximal ion density crossed by the particle and N_i^0 is the initial ion density first crossed by the particle in the model. $N_i^{injector}$ has been estimated from post-discharge current between 10^{15} and 10^{16} m^{-3} depending on applied voltage and discharge gap. The ion density along the particle trajectory increases up to N_i^m (cf. fig. S5 and §4.1 of SI), and then it decreases until reaching the ion trap. N_i^m has then been estimated from equation (S2 in SI) as between 8×10^{14} and 5×10^{15} m^{-3}, with a transit time of 5×10^{-5} s (required to cross the 4 mm from the ion injector to the aerosol flux, with a mean velocity of 79 m s^{-1}). The calculations are thus handled for initial ion density N_i^0 between 10^{12} and 10^{16} m^{-3} neglecting the initial phase of increasing ion density.

Calculations of the mean ion density over a cross section of the axisymmetric post-corona charger take into account self-repulsion only as if there is no particle ($n_{i\ wo\_part}$ given by eq. 3), self-repulsion and ion consumption for aerosol charging ($n_{i\ w\_part}$ eq. 4) or self-repulsion, ion consumption for aerosol charging as well as aerosol space charge (eq. 5):

$$\frac{dn_{i\,wo\_part}}{dt} = -\frac{Z_i.e}{\varepsilon_0} n_{i\,wo\_part}^2 \quad (t) \tag{3}$$

$$\frac{dn_{i\,w\_part}}{dt} = -\frac{Z_i.e}{\varepsilon_0} n_{i\,w\_part}^2 \quad (t) - \frac{dq_p(t)}{dt} \cdot e \cdot n_p(t) \tag{4}$$

$$\frac{dn_i}{dt} = -\frac{Z_i.e}{\varepsilon_0} \Big(n_i(t) + q_p(t) \cdot n_p(t)\Big)^2 - \frac{dq_p(t)}{dt} \cdot e \cdot n_p(t) \tag{5}$$

Charge distributions are calculated using Fuchs' charging theory which is valid in the transition regime (i.e. for $K_{ni} = 2\lambda_i/d_p \approx 1$ with, at atmospheric pressure, $\lambda_i \approx 15$ nm (Bricard 1949)). Biskos et al. 2005 shows good agreement between experimental results and Fuchs theory in the range $10 < d_p < 300$ nm and up to 500 nm between Monte Carlo simulation and Fuchs theory. The temporal evolution of the charge distribution of monodispersed aerosol is described by a set of differential equations, given by the birth-and-death model (Boisdron and Brock 1970).

$$\frac{dn_p^q}{dt} = \beta_{q-1} \cdot n_p^{q-1} \cdot n_i - \beta_q \cdot n_p^q \cdot n_i \tag{6}$$

where N_p^q is the concentration of particle with q the number of elementary charges (for $q \geq 0$) and β_q the attachment coefficient of ions on a particle with q charges calculated using Fuchs' theory as detailed in section S2.4 of the SI. Calculations are carried out by iteration of discrete time steps.

Fig. 5 represents the temporal evolutions of the calculated ion density in the worst case (i.e. for the 350 nm particles collecting more ions than the 91 nm ones) for an initial ion density, N_i^0 of 10^{16} m^{-3} to reach the measured mean charge per particle after 50 ms.

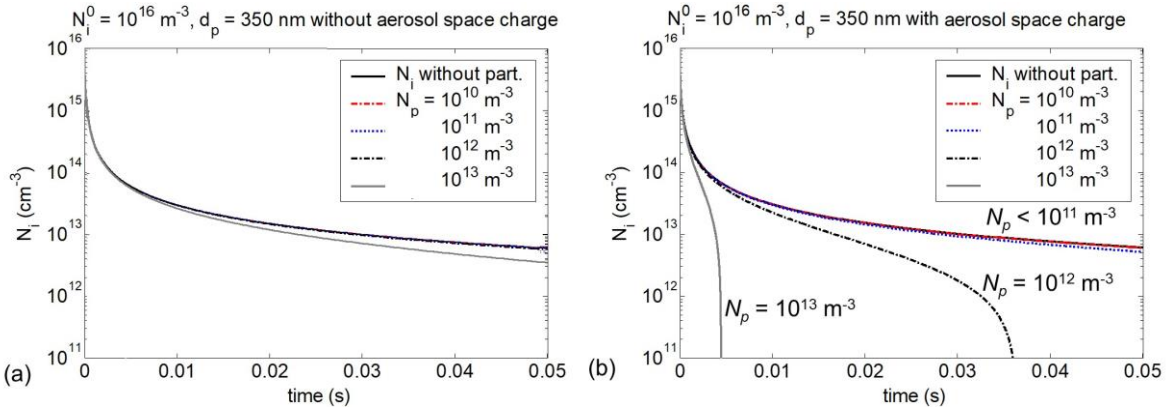

Fig. 5. Temporal evolution of post-discharge ion density calculated for different aerosol concentrations with d_p = 350 nm and a maximal ion density, N_i^0 = 10^{16} m^{-3} taking into account: (a) ion consumption for aerosol charging and (b) ion consumption as well as aerosol space charge

As expected, Fig. 5a confirms that the effect of ion consumption for aerosol charging on ion density is negligible for 350 nm aerosol with concentration below 10^{13} m^{-3} over the first 50 ms. The effects of aerosol space charge and ion consumption are negligible for $N_p < 10^{12}$ m^{-3}, as the temporal evolution of ion density is unaffected by aerosol concentration (see Fig. 5b). For larger particle concentration, the reduction of ion density is no longer negligible and charging conditions depend on aerosol concentration. It has to be underlined that the reduction of the $N_i \times \tau$ occurs for aerosol concentration at least three orders of magnitude higher for the model (higher than 10^{12} m^{-3}) than for the experiments (for N_p lower than 4.7×10^{11} m^{-3} cf. Table 2).

3.2.2 Calculations of charge evolution with aerosol concentration in axial geometry

Based on this model, the evolutions of charge distribution are plotted in Fig. 6a, versus aerosol concentration for a given diameter, as well as the mean charge in Fig. 6b, for different particle diameters from 10 nm to 1 µm. The aerosol concentration lies between 10^9 (the mean charge per particle is constant for lower concentration than 10^9 m^{-3}) and 10^{16} m^{-3}.

We have arbitrarily defined the maximal aerosol concentration, N_p^{max}, which for the mean charge per particle is at least 90% of the maximal one achieved at low concentration (dotted grey line in Fig. 6(b) with black dots).

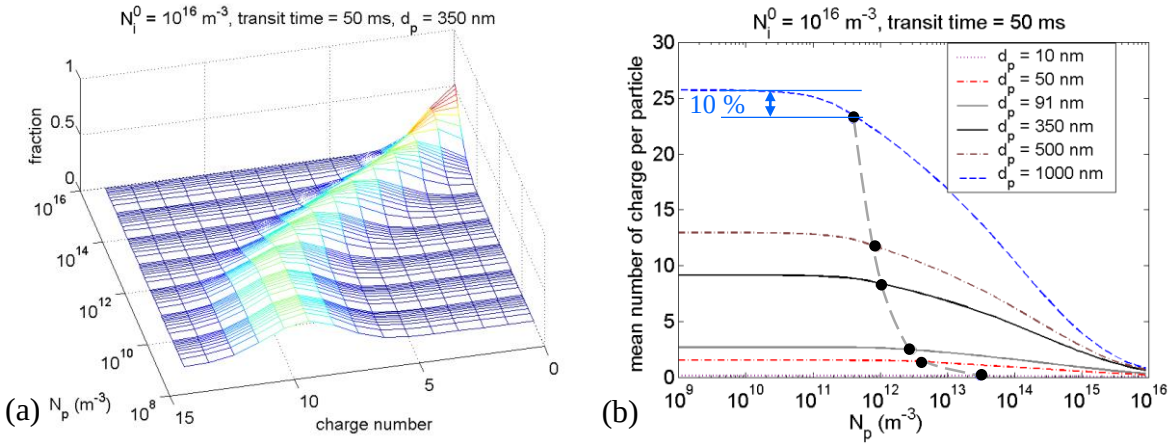

Fig. 6. Evolutions of the charge per particle as a function of aerosol concentration (N_p) calculated from Eq. 5: (a) charge distribution for 350 nm particle, (b) mean charge per particle calculated for particle size between 10 and 1000 nm, charged for 50 ms with initial ion density of 10^{16} m^{-3} (● defines the N_p^{max} with 90 % of the maximal mean charge per particle q_p^{max}).

The particle charge distribution is constant for aerosol concentration lower than 10^{11} m^{-3} (cf. Fig. 6a) with subsequent constant mean charge per particle for 350 nm particles (cf. Fig. 6b). As for experimental results, the mean charge per particle decreases with increasing aerosol concentration. For a 50 ms charging time, the reduction of aerosol mean charge occurs for aerosol concentration that depends on particle size (cf. Fig. 6b): above 10^{10} m^{-3} for 1 µm particle, above 10^{11} m^{-3} for 350 nm particle and above 5×10^{11} m^{-3} for 91 nm. The calculated reduction of ion density with increasing aerosol concentration shows that the reduction of aerosol mean charge is partly due to the consumption of ions by particle. Nevertheless, with an initial ion density N_i^0 of 10^{16} m^{-3}, calculations show that the ion density profile is affected more by aerosol space charge than by ion consumption in an axisymmetric charger with homogeneous mixing of ions and particles. The same calculations have been done for N_i^0 between 10^{12} and 10^{16} m^{-3}. For initial ion density lower than 10^{15} m^{-3}, the effect of ion consumption is dominant as aerosol space charge is less intense due to lower mean charge per particle.

These calculations can be used to analyze the case of asymmetric mixing conditions at least at the beginning of the charging zone, which is critical; because, in this region, any modification of ion density would affect the ion density in the whole charging volume and aerosol charging rate is maximal. For aerosol concentration below 10^{10} m^{-3}, ion consumption has a negligible effect on the mean charge per particle and cannot explain the results reported in fig. 4b. Below 10^{10} m^{-3} the mean charge per particle is maximum showing that most of the particles interact with very high ion density that can only be altered by aerosol space charge.

Moreover, calculations show that the reduction of the aerosol mean charge occurs in axial geometry for concentrations higher than those experimentally available for monodisperse aerosol. The reduction of the mean charge measured with chargers without axial symmetry occurs for concentration as low as 10^9 m^{-3} much lower than for the calculations, this demonstrates the critical role of the symmetry of the charger.

3.2.3 Maximal aerosol concentration for negligible influence of aerosol concentration on the mean charge

A trivial condition on the minimal ion density can be introduced by assuming homogeneous ion density to limit the evolution of ion density related to ion collision with particle typically $N_i >> N_p$ (Cooper and Reist 1973). Without ion generation or loss except for consumption by particles, the difference between the ion densities at the inlet and the outlet of the charging volume is $\overline{q_p^{final}} \cdot N_p$ with q_p the mean number of charge per particle assuming negligible initial mean charge. Thus, the initial ion density (N_i^0) should fulfil the following condition to limit ion density reduction below x %: $N_{i\ min}^0 > 100\,x \cdot \overline{q_p^{final}(d_p)} \cdot N_p$. Next, we shall focus on the influence of aerosol concentration in decreasing ion density controlled by space charge repulsion in a charging volume with axial symmetry.

The calculated values of maximal aerosol concentration (N_p^{max} as defined in §3.2.2) are plotted as a function of particle diameter in Fig. 7 (a) for different charging conditions. Initial ion density and transit time depends on the application. The range of parameters corresponds to classical values for corona charger and includes the experimental conditions (50 ms charging time and $N_i^{injector}$ between 10^{15} and 2×10^{16} m^{-3}).

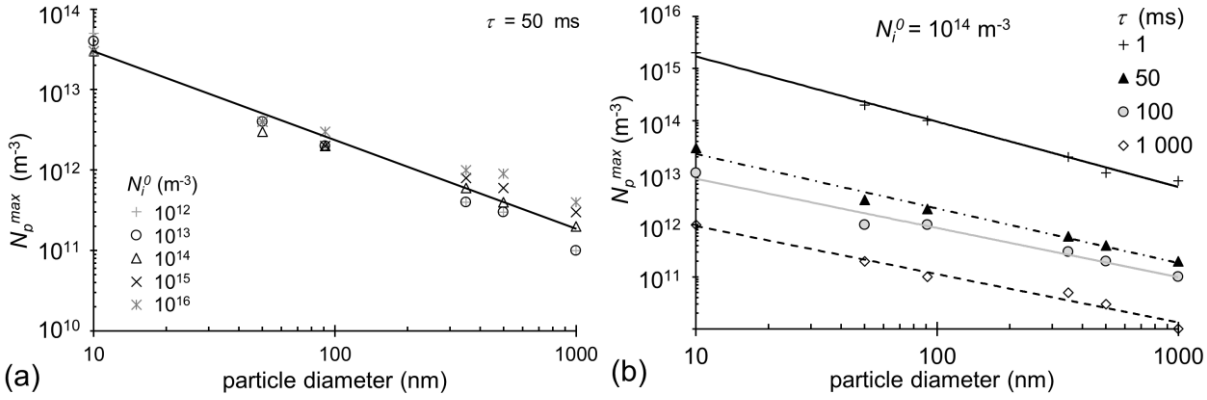

Fig. 7. Maximal aerosol concentration Npmax for constant mean charge per particle within 10 % as a function of particle diameter (a) for a given charging time of τ = 50 ms and initial ion density N_i^0 from 10^{12} to 10^{16} m^{-3} and (b) for a given initial ion density N_i^0 = 10^{14} m^{-3} with charging times between 1 ms and 1 s.

First, it has to be reminded that $N_i \times \tau$ controls the mean charge per particle so that different initial ion density or transit time lead to different final mean charge per particle. Moreover, most aerosol chargers operate with a large excess of ions per particle, despite some theoretical cases treated here. The maximal aerosol concentration, N_p^{max} decreases for larger particles and longer charging times as more ions are consumed by the particles and aerosol space charge is larger. A surprising result is that the maximal aerosol concentration, N_p^{max} is, as a first approximation, independent of the initial ion density, N_i^0 (cf. Fig. 7). This is even true when aerosol concentration exceeds ion density leading to a mean charge per particle lower than 1 as only a fraction of the particle can be charged. N_p^{max} is nearly independent of N_i^0 but discrepancies arise when the particle diameter and the related attachment coefficients of ions with particle increase. For particles of 1 µm, N_p^{max} evolves by a factor 3 with initial ion density between 10^{12} and 10^{16} m^{-3}.

For higher N_i^0, one would expect a higher N_p^{max}, but three facts limit the discrepancies. For higher N_i^0, (i) the ion density decreases faster (cf. §4.1 of SI), (ii) the ion flux on particle is higher so that particles get charged sooner and (iii) more ions are consumed by the particles, than for lower N_i^0.

Thus, at first approximation, the maximal aerosol concentration for a constant mean charge per particle only depends on aerosol transit time and particle size. All the calculated N_p^{max} (charging time τ between 1 ms and 1 s, particle size 10 nm - 1 µm and initial ion density 10^9 - 10^{16} m^{-3}) values follow the relation $4\times10^3 < N_p^{max}.d_p.\tau < 25\times10^3$ ($s.m^{-2}$). As a rule of thumb, to limit the effect of aerosol concentration on the mean charge per particle (below 10 % of the maximal mean charge reach at low aerosol concentration) for the case of heterogeneous ion density profiles, the aerosol concentration should fulfill:

$$N_p < \frac{25\cdot10^4}{d_p.\tau} \quad (7)$$

with N_p in m^{-3}, d_p in m and τ in s. For instance, the theoretical value of maximal aerosol concentration of 350 nm particle for a charging time of 50 ms is about 10^{12} m^{-3}.

Aerosol chargers devoted to nanoparticle charging with high aerosol penetration and transit time shorter than 0.1 s are thus not concerned by this limit. Nevertheless, for particles larger than 500 nm, the charging time could be adapted to the aerosol size and concentration to get rid of the effects of aerosol concentration on the final mean charge per particle downstream post-corona diffusion charger, using this criterion. Otherwise, the evolution of the final mean charge per particle versus aerosol concentration should be taken into account for accurate data inversion from electrical mobility spectra to size distribution.

4 Conclusions

The effect of aerosol space charge on the mean charge per particle should be taken into account to design diffusion aerosol chargers devoted to achieving well-defined mean charge per particle and size-charge relation (e.g. for aerosol measurement tool or electrostatic processing of aerosol).

For particles larger than 500 nm and concentration higher 10^{13} m^{-3} injected downstream a corona discharge at less than 4 mm from ion injection, the aerosol space charge limit the ion flux injected in the post-corona charging volume by a few percent.

The consumption of ions for aerosol charging, which reduces the free ions concentration available to charge the particles and thus the $N_i\times\tau$, only affects the mean charge per particle for concentrations higher than 10^{12} m^{-3}, which is above the experimentally available concentrations for monodisperse aerosol.

Both experimental results and calculations support the notion that, for initial ion density higher than 10^{15} m^{-3}, electrostatic repulsions of ions by the space charge including ions and less mobile charged aerosols, mainly accounts for the spatial ion redistribution and the related lower charge per particle at higher aerosol concentration.

To limit the effect of aerosol space charge on the charging conditions, an axial symmetry of the charger with a core of ions surrounded by particles at the inlet section of the charging volume is optimal in terms of ion-aerosol mixing (as already demonstrated by Alonso et al. 2009, patented in 2012 and confirmed by Domat et al. 2014). In this geometry, aerosols are injected into ion density higher than 10^{15} m^{-3}, few mm from the ion injection, with all ions forced by self-repulsion to cross the aerosol flow.

In post-corona chargers with axisymmetric ion-aerosol mixing conditions, the measured mean charge per particle of a given diameter is constant whatever the concentration up to at least 10^{11} m^{-3}. The maximal aerosol concentration which for the mean charge per particle remains constant has been calculated for aerosol particles with diameters between 10 nm and 1 µm, for charging time between 1 ms and 1 s and initial ion density between 10^9 and 10^{16} m^{-3}. The maximal aerosol concentration depends on aerosol diameter and charging time but is nearly independent of initial ion density. A simple expression has thus been established to define the maximal aerosol concentration.

On the contrary, in post-corona chargers without axial symmetry of ion-aerosol mixing, the effect of aerosol concentration is to decrease the final mean charge per particle by up to a factor 10 for aerosol concentrations from 10^9 to 10^{13} m^{-3}. The reduction in charge occurs for concentrations as low as a few 10^9 m^{-3}. Nevertheless, aerosol chargers with transverse jets of ions and aerosols in crossflow can be an asset for specific applications to overcome the limits of existing aerosol chargers, since the effect of aerosol concentration on the mean charge per particle can be limited. These chargers can lead to charge-diameter relation that differs from classical ones to improve the selection of aerosol size range by differential mobility analyzer.

Funding: This work was supported by CNRS contracts with EDF 1997-2001 [M25/B64117/EL855]; RAMEM 2007-2010 [UMR8578/025101]; and IRSN 2010-2016 [UMR8578/053233].

References

Adachi, M., K. Okuyama, Y. Kousaka, H. Kozuru, D. Y. H. Pui. 1987. Diffusion charging of ultrafine aerosol-particles by positive helium, argon and nitrogen ions. *J. Appl. Phys.* 62:3050-3052. doi: 10.1063/1.339368.

Alonso, M. and F. J. Alguacil. 2003. The effect of ion and particle losses in a diffusion charger on reaching a stationary charge distribution. *Journal of Aerosol Science* 34:1647-1664. doi.

Alonso, M., F. J. Alguacil, J. P. Borra. 2009. A numerical study of the influence of ion-aerosol mixing on unipolar charging in a laminar flow tube. *Journal of Aerosol Science* 40:693-706. doi: 10.1016/j.jaerosci.2009.04.004.

Alonso, M., V. Gomez, J. P. Borra. 2014. Determination of the mean mobility of aerosol nanoparticles classified by differential mobility analyzers. *Aerosol Science and Technology* 48:1217-1225. doi.

Alonso, M. and C. H. Huang. 2015. High-efficiency electrical charger for nanoparticles. *Journal of Nanoparticle Research* 17:332. doi: 10.1007/s11051-015-3137-8.

Alonso, M., M. I. Martin, F. J. Alguacil. 2006. The measurement of charging efficiencies and losses of aerosol nanoparticles in a corona charger. *Journal of Electrostatics* 64:203-214. doi.

Biskos, G., E. Mastorakos, N. Collings. 2004. Monte-carlo simulation of unipolar diffusion charging for spherical and non-spherical particles. *Journal of Aerosol Science* 35:707-730. doi: http://dx.doi.org/10.1016/j.jaerosci.2003.11.010.

Biskos, G., K. Reavell, N. Collings. 2005. Unipolar diffusion charging of aerosol particles in the transition regime. *Journal of Aerosol Science* 36:247-265. doi: http://dx.doi.org/10.1016/j.jaerosci.2004.09.002.

Boisdron, Y. and J. R. Brock. 1970. On the stochastic nature of the acquisition of electrical charge and radioactivity by aerosol particles. *Atmospheric Environment (1967)* 4:35-50. doi: https://doi.org/10.1016/0004-6981(70)90052-1.

Borra, J.-P., N. Jidenko, M. Alonso. 2012. Concentric electrical discharge aerosol charger: Patent WO/2014/102258, Centre national de la recherche scientifique (CNRS) (3 rue Michel Ange, Paris, Paris, F-75016, FR).

Borra, J.-P., N. Jidenko, E. Bourgeois. 2009. Atmospheric pressure plasmas for aerosols processes in materials and environment. *The European Physical Journal Applied Physics* 47:22804. doi.

Borra, J. P. 2006. Nucleation and aerosol processing in atmospheric pressure electrical discharges: Powders production, coatings and filtration. *Journal of Physics D: Applied Physics* 39:R19-R54. doi.

Borra, J. P., A. Goldman, M. Goldman, D. Boulaud. 1998. Electrical discharge regimes and aerosol production in point-to-plane dc high-pressure cold plasmas: Aerosol production by electrical discharges. *Journal of Aerosol Science* 29:661-674. doi.

Bouarouri, A. 2014. Développement d'un chargeur à décharge couronne pour la mesure à 10 hz de la concentration d'un aérosol atmosphérique: PhD thesis of University Paris-Saclay.

Bouarouri, A., N. Jidenko, F. Gensdarmes, D. Maro, D. Boulaud, J. P. Borra. 2016. Ion current density profiles in negative corona gaps versus ehd confinements. *Journal of Electrostatics* 82:88-95. doi: http://dx.doi.org/10.1016/j.elstat.2015.08.005.

Bricard, J. 1949. L'équilibre ionique de la basse atmosphère. *Journal of Geophysical Research* 54:39-52. doi.

Chen, X., J. Jiang, D.-R. Chen. 2019. Maximizing the singly charged fraction of sub-micrometer particles using a unipolar charger. *Aerosol Science and Technology* 53:990-997. doi: 10.1080/02786826.2019.1617833.

Choi, Y. and S. Kim. 2007. An improved method for charging submicron and nano particles with uniform charging performance. *Aerosol Science and Technology* 41:259-265. doi: 10.1080/02786820601148262.

Cooper, D. W. and P. C. Reist. 1973. Neutralizing charged aerosols with radioactive sources. *Journal of Colloid and Interface Science* 45:17-26. doi: 10.1016/0021-9797(73)90239-7.

de La Verpilliere, J. L., J. J. Swanson, A. M. Boies. 2015. Unsteady bipolar diffusion charging in aerosol neutralisers: A non-dimensional approach to predict charge distribution equilibrium behaviour. *Journal of Aerosol Science* 86:55-68. doi: http://dx.doi.org/10.1016/j.jaerosci.2015.03.006.

Domat, M., F. E. Kruis, J. M. Fernandez-Diaz. 2014a. Determination of the relevant charging parameters for the modeling of unipolar chargers. *Journal of Aerosol Science* 71:16-28. doi.

Domat, M., F. E. Kruis, J. M. Fernandez-Diaz. 2014b. Investigations of the effect of electrode gap on the performance of a corona charger having separated corona and charging zones. *Journal of Aerosol Science* 68:1-13. doi.

Flagan, R. C. 1998. History of electrical aerosol measurements. *Aerosol Science and Technology* 28:301-380. doi: 10.1080/02786829808965530.

Fuchs, N. A. 1963. On the stationary charge distribution on aerosol particles in a bipolar ionic atmosphere. *Pure and Applied Geophysics* 56:185-193. doi.

Hewitt, G. W. 1957. The charging of small particles for electrostatic precipitation. *Transactions of the American Institute of Electrical Engineers, Part I: Communication and Electronics* 76:300-306. doi: 10.1109/TCE.1957.6372672.

Hoppel, W. A. and G. M. Frick. 1988. Aerosol charge distributions produced by radioactive ionizers, Medium: X; Size: Pages: 42.

Huang, C.-H. and M. Alonso. 2012. Influence of particle location on the number of charges per charged nanoparticle at the outlet of a needle charger. *Journal of the Air & Waste Management Association* 62:87-91. doi: 10.1080/10473289.2011.617609.

Intra, P. and N. Tippayawong. 2011. An overview of unipolar charger developments for nanoparticle charging. *Aerosol and Air Quality Research* 11:187-209. doi: 10.4209/aaqr.2010.10.0082.

Intra, P., A. Yawootti, P. Rattanadecho. 2017. Corona discharge characteristics and particle losses in a unipolar corona-needle charger obtained through numerical and experimental studies. *Journal of Electrical Engineering & Technology* 12:2021-2030. doi: 10.5370/jeet.2017.12.5.2021.

Jayaratne, E. R., X. Ling, B. Pushpawela, L. Morawska. 2019. Experimental determination of the dispersion of ions from a point source in the environment. *Environmental Technology* 40:1213-1222. doi: 10.1080/09593330.2017.1418912.

Jiang, J., M.-H. Lee, P. Biswas. 2007. Model for nanoparticle charging by diffusion, direct photoionization, and thermionization mechanisms. *Journal of Electrostatics* 65:209-220. doi.

Jidenko, N., A. Bouarouri, F. Gensdarmes, D. Maro, D. Boulaud, J. P. Borra. 2020. Post-corona unipolar chargers with tuneable aerosol size-charge relations: Parameters affecting ion dispersion and particle trajectories for charger designs. *Aerosol Science and Technology*:1-12. doi: 10.1080/02786826.2020.1817310.

Jidenko, N., D. Maro, F. Gensdarmes, D. Boulaud, J.-P. Borra. 2012. Sub-second diffusion charging, in *European Aerosol Conference*. Grenada, Spain.

Laitinen, A. and J. Keskinen. 2016. Performance of a sonic jet-type charger in high dust load. *Journal of Electrostatics* 83:1-6. doi: 10.1016/j.elstat.2016.06.002.

Liu, B. Y. H. and A. Kapadia. 1978. Combined field and diffusion charging of aerosol particles in the continuum regime. *Journal of Aerosol Science* 9:227-242. doi.

Liu, B. Y. H., D. Y. H. Pui, W. O. Kinstley, W. G. Fisher. 1987. Aerosol charging and neutralization and electrostatic discharge in clean rooms. *Journal of Environmental Sciences* 30:42-46. doi.

Marlow, W. H. and J. R. Brock. 1975. Unipolar charging of small aerosol particles. *Journal of Colloid and Interface Science* 50:32-38. doi.

Medved, A., F. Dorman, S. L. Kaufman, A. Pöcher. 2000. A new corona-based charger for aerosol particles. *Journal of Aerosol Science* 31, Supplement 1:616-617. doi.

Nishida, R. T., N. M. Yamasaki, M. A. Schriefl, A. M. Boies, S. Hochgreb. 2019. Modelling the effect of aerosol polydispersity on unipolar charging and measurement in low-cost sensors. *Journal of Aerosol Science* 130:10-21. doi: https://doi.org/10.1016/j.jaerosci.2019.01.003.

Nolan, P. J. and E. Kuffel. 1957. Metal point discharge nuclei and the production of multiply charged ions from condensation nuclei. *Geofisica pura e applicata* 36:201-210. doi: 10.1007/bf01993008.

Park, D., M. An, J. Hwang. 2007. Development and performance test of a unipolar diffusion charger for real-time measurements of submicron aerosol particles having a log-normal size distribution. *Journal of Aerosol Science* 38:420-430. doi: http://dx.doi.org/10.1016/j.jaerosci.2007.01.003.

Pui, D. Y. H., S. Fruin, P. H. McMurry. 1988. Unipolar diffusion charging of ultrafine aerosols. *Aerosol Science and Technology* 8:173-187. doi: 10.1080/02786828808959180.

Qi, C. and P. Kulkarni. 2012. Unipolar charging based, hand-held mobility spectrometer for aerosol size distribution measurement. *Journal of Aerosol Science* 49:32-47. doi: http://dx.doi.org/10.1016/j.jaerosci.2012.02.005.

Reischl, G. P., J. M. Mäkelä, R. Karch, J. Necid. 1996. Bipolar charging of ultrafine particles in the size range below 10 nm. *Journal of Aerosol Science* 27:931-949. doi: http://dx.doi.org/10.1016/0021-8502(96)00026-2.

Tigges, L., A. Jain, H. J. Schmid. 2015. On the bipolar charge distribution used for mobility particle sizing: Theoretical considerations. *Journal of Aerosol Science* 88:119-134. doi.

Unger, L. 2001. Charge d'aérosols par décharge électrique pour la filtration d'effluents particulaires. Orsay: PhD thesis of Université Paris Sud.

Unger, L. and J.-P. Borra. 2000. Dimensionnement d ‘une décharge électrique pour l’optimisation de la charge des aérosols, in *16ème congrès Français sur les Aérosols*, pp 68-73. Paris.

Veshchunov, M. S. 2021. On the saturation of unipolar and bipolar diffusion charging of aerosols. *Aerosol Science and Technology* 55:2-11. doi: 10.1080/02786826.2020.1807460.

Vivas, M. M., E. Hontañón, A. Schmidt-Ott. 2008. Reducing multiple charging of submicron aerosols in a corona diffusion charger. *Aerosol Science and Technology* 42:97-109. doi: 10.1080/02786820701787969.

Whitby, K. T. 1961. Generator for producing high concentrations of small ions. *Rev. Sci. Instrum.* 32:1351-1355. doi.

Whitby, K. T., B. Y. H. Liu, C. M. Peterson. 1965. Charging and decay of monodispersed aerosols in presence of unipolar ion sources. *Journal of Colloid Science* 20:585-&. doi: 10.1016/0095-8522(65)90037-1.

White, H. J. 1951. Particle charging in electrostatic precipitation. *Trans. Am. Inst. Electr. Eng.* 70:1186-1191. doi.

Zheng, C. H., Q. Y. Chang, Q. Y. Lu, Z. D. Yang, X. Gao, K. F. Cen. 2016. Developments in unipolar charging of airborne particles: Theories, simulations and measurements. *Aerosol and Air Quality Research* 16:3037-3054. doi: 10.4209/aaqr.2016.07.0319.

Effect of aerosol concentration on post-corona unipolar diffusion charging: ion density retro-controlled by aerosol space charge versus geometry of ions-aerosols mixing

N. Jidenko, A. Bouarouri & J.-P. Borra
Université Paris-Saclay, CNRS, Laboratoire de physique des gaz et des plasmas, 91405, Orsay, France.

Supplementary information

1 Introduction

The supplementary information summarizes the relation between operating conditions and physical processes that control the charging conditions (ion density on each point of the charging volume and particle trajectory in these ion densities) as previously done in other arrangements of post-corona diffusion chargers (Bouarouri 2014; Jidenko et al. 2020; Jidenko et al. 2012; Unger 2001). The main objectives are to present the electrical characterization of the perpendicular 1 charger and to identify the critical processes to be implemented in the simplified model (cf. section 3.1).

2 Additional setup

This section addresses the electrical characterization of the perpendicular 1 charger and the consequence of Trichel pulse on post-discharge ion current as well as additional post-discharge corona charger geometries.

2.1 Discharge and post-discharge currents without particles

The discharge takes place at the vicinity of the negative point, for electric field higher than the threshold ionization field (of about 3 MV m^{-1} for dry air, at atmospheric pressure). Electrons are then attached on gas molecule within a few tens of ns to form negative ions drifting in the gap. The electric field in the gap is retro-controlled by the negative space charge that prevents from spark discharge to occur for discharge current below 100 µA, in air at 1030 hPa.

Below the onset spark voltage, auto-stabilization, Trichel and corona regimes follow each other at increasing applied voltage. In the Trichel regime, the instantaneous current includes pulses below 2 mA, for 100 ns duration, at frequency from 10 kHz to 10 MHz (Dordizadeh, Adamiak and Castle 2016) whereas the current is constant in the corona regime. A transition regime characterized by trains of Trichel pulses superimposed over a continuous corona current (cf. Trichel-corona mix in Fig. S1a) occurs between Trichel and Corona regimes depending on the external circuit (value of the resistor in the circuit). In such unstable discharge condition, fluctuating ion flux is injected from the corona ion source in the charging volume. All the measurements have thus been carried out in Trichel or Corona regimes excluding the transition regime.

The discharge current, (I_d in Fig. S1a) and post-discharge ion current (I_i^{wall} in Fig. S1b) are plotted for gap lengths of 5, 7 and 9 mm as a function of needle voltage and discharge current respectively (both negative voltage and current are plotted in absolute values). I_i^{wall} has been measured, without particle, with an aerosol gas flowrate of 7 L min^{-1}. At constant pressure in the discharge gap, the effect of the aerosol flow rate on I_i^{wall} is negligible (reduction of 0.5 % due to the confinement of the ion space charge close to the ion injection in the charging volume).

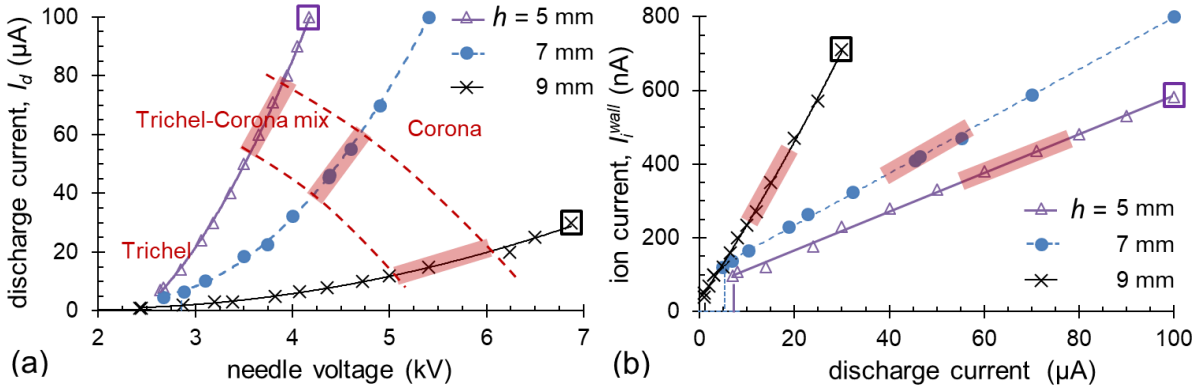

Figure S1. Characterization of the ion source without aerosol (a) discharge current (I_d) versus voltage and (b) post-discharge ion current measured on the metal wall of the charging volume (I_i^{wall}) versus I_d for gap lengths of 5, 7 and 9 mm (air at 20°C, 1030 hPa, point radius = 80 µm, hole diameter = 2 mm, Q_i = 15 L min^{-1} Q_a = 7 L min^{-1}).

The corona voltage ranges and voltage required to reach the same discharge current both increase with larger gap. As expected for corona regimes, the ratio I_d/V_d is linear with V_d (Akishev et al. 2001; Goldman and Goldman 1978).

In these operating conditions, the post-discharge ion current linearly increases with the discharge current (cf. Fig. S1b). For a given discharge current I_d, the post-discharge ion current increases with increasing gap length between 5 to 9 mm. This result may seem surprising as post-discharge ion current is related to the ion current density on the plane in the gap above the hole which is, for a corona discharge without wall, proportional to $I_d/(2d^2)$ (Goldman, Goldman and Sigmond 1985). Ions are confined above the extraction hole by the electric field generated by the surface potential on the insulating walls of the discharge (cf. Fig.2) and by the gas flow around the needle (Bouarouri et al. 2016; Kimoto et al. 2010). The trends in Fig. S1b are due to the fact that the intensity of the confinement depends on the gap length.

2.2 Consequence of Trichel pulse on post-discharge ion current

In the Trichel regime, the instantaneous discharge current includes regular train of current pulses of about 1 mA height with a duration of 100 ns at frequency from 10 kHz to 10 MHz depending on the applied voltage (Dordizadeh, Adamiak and Castle 2016; Goldman and Goldman 1978; Trichel 1938). What are the consequences of the Trichel pulses in terms of ion flux entering the charging volume? The instantaneous post-discharge ion current, I_i^{wall} also contains current pulses (in phase with the discharge current pulse related to Trichel pulse). Nevertheless, these pulses are due to a displacement current induced by electron motion near the point. Actually, the same pulses are measured with a reverse gas flow (from the charging volume to the discharge volume) with a mean post-discharge ion current I_i^{wall} below the detection limit of 10 fA. Thus, the ions flux can be considered as constant and the pulses should not be taken into account in the post-discharge ion current. Nevertheless, the contribution of the displacement current to the Trichel pulse represents less than 15% of I_i^{wall} and can be neglected.

2.1 Other post-corona charger arrangements

The schemes of the post-corona diffusion chargers used for the data presented in Table S1 are detailed below. The arrangement 1 corresponds to the geometry of the post-corona aerosol charger presented in the paper. Three other arrangements, in which the effect of aerosol concentration on the mean charge per particle has been measured, are presented on Fig. S2, S3 and S4.

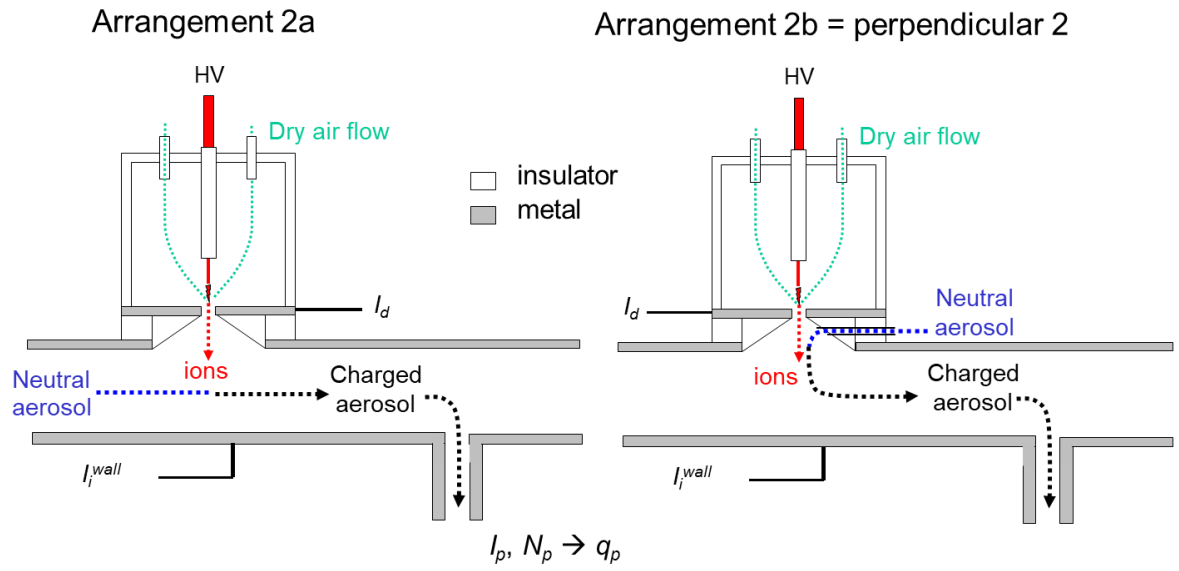

Figure S2. Post-corona diffusion chargers from Unger 2001 to study the influence of the location of aerosol injection on the mean charge per particle

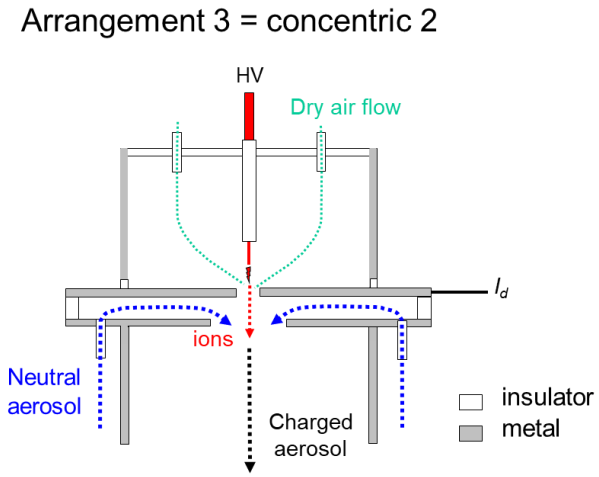

Figure S3. Post-corona diffusion charger from Bouarouri 2014 to study the influence of the initial ion density on the mean charge per particle based on (Borra, Jidenko and Alonso 2012).

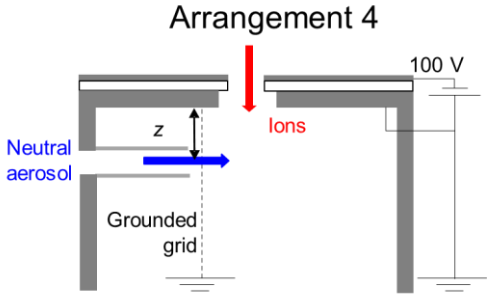

Figure S4. Scheme of post-corona diffusion charger from Bouarouri 2014 to study the influence of the location of aerosol injection on the mean charge per particle.

Some of the experimental results obtained with the arrangements given in Fig. S1, S2 and S3 are detailed on Table S1.

3 Effect of aerosol concentration on the mean charge per particle in the arrangement 2b

A unimodal aerosol of DEHS is generated by a nebulizer with a modal diameter of 0.3 µm and a mean diameter of 0.6 µm.

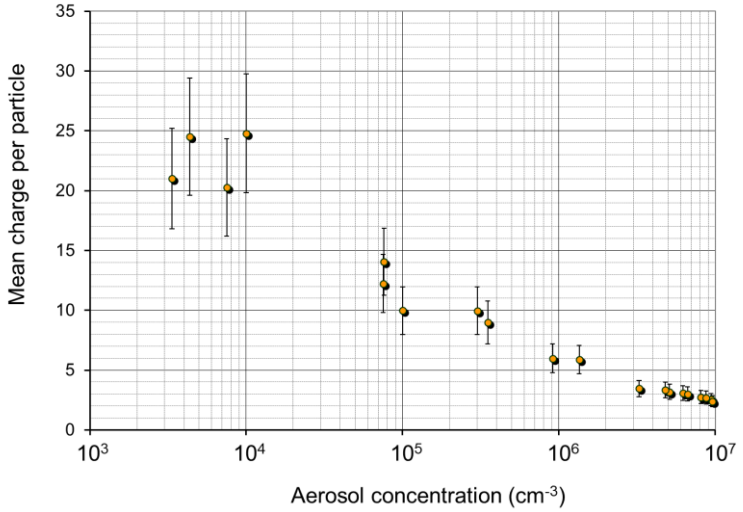

Figure S5: Effect of aerosol concentration on the mean charge per particle in the arrangement 2a V_d = -6.5 kV, I_d = 100 µA, gap length = 4 mm, diameter of ion orifice = 0.5 mm, Q_{ion} = 3 L.min^{-1}, $Q_{aerosol}$ = 6.6 L.min^{-1}.

The mean charge per particle decreases from 25 to 2.5 with aerosol concentration from 4×10^3 cm^{-3} to 10^7 cm^{-3} (Unger 2001). This initial result has been reproduced in the other charger arrangements with monodispersed aerosol.

4 Main physical processes that control the charging conditions

Whatever the considered diffusion charging law, the mean charge per particle depends on three sets of parameters: ions properties (electrical mobility, Z_i; mass and density, N_i), aerosol properties (diameter, d_p) and gas properties (temperature). For a given aerosol diameter, in a constant ion density, the critical parameter that controls the final mean charge per particle is the $N_i\times\tau$ product.

The $N_i\times\tau$ product can be defined as the average for many particle of the $N_i\times t$ along each particle trajectory:

$$N_i\times\tau \;= \frac{1}{N}\sum_{k=1}^{N}\int_{along\ k\ particle\ trajectory} N_i^k(t)\cdot dt \qquad \text{(S1)}$$

with N_i^k the ion density in which the k^{th} particle passes through.

In a real aerosol charger, the ion and aerosol transport is critical. Based on simplifying assumptions; the $N_i\times\tau$ can be estimated from ion current measurement to evaluate ion density distribution as well as from gas velocity and electric field to evaluate the mean particle trajectory. In most cases, the final mean charge per particle allows one to calculate the $N_i\times\tau$ using a charging law assuming negligible losses of charged aerosol. In best cases, electro-hydrodynamics model of ion and aerosol transport neglecting some physical processes or assuming initial condition allows one to evaluate $N_i\times\tau$. The following sections summarize the physical processes that affects aerosol-charging conditions.

4.1 Ions properties

The electrical mobility distribution of negative ions in post-discharge is bimodal and evolves with the transit time. Nevertheless, ion electrical mobility and mass do not evolve more than 10% for given gas composition, temperature and pressure. Moreover, the charging law is not very sensitivity to these parameters (Reischl et al. 1996). Thus, at first approximation, a mean ion mass and a mean ion electrical mobility can be used for calculation as already proven for bipolar charging (Gopalakrishnan et al. 2013).

The ion density distribution in the charging volume is more critical as the initial ion density can be tuned over at least one order of magnitude by the discharge voltage and the gas flow rate injected in the discharge. For a defined charging volume, the stationary spatial ion density distribution in the charging volume depends on the ion flux entering the charging volume, on electro-hydro-dynamic processes related to gas flow velocity and electric field (Borra, Jidenko and Bourgeois 2009; Borra 2008). For instance, without insulator plane with concentric ion-aerosol injection (cf. Table S3), the mean charge per particle of 460 nm evolves from 17 to 21 elementary charge with the discharge current from 8 µA to 100 µA

To illustrate the influence of initial ion density, $N_i°$ on the mean charge per particle, Fig. S6 represents the calculations of ion density and the mean charge per particle of 350 nm for two initial ion densities of $N_i° = 3\times10^{14}$ and 10^{16} m^{-3} (the estimation of $N_i°$ is presented in section 3.4 of the paper). Calculations are based on White's law in decreasing ion density controlled by ion space charge repulsion assuming plug flow and constant radial ion density and aerosol concentration in the tube charging volume. Townsend have first derived equations giving the time rate of deposition of ion in the absence of any external electric field. The stationary ion density as a function of time or distance from the generator is (Bouarouri 2014; Townsend 1898; Unger and Borra 2000; Whitby 1961):

$$N_{i\ withtout\ particle}(t) = \frac{N_i^0}{1+t/\tau_i}, \text{ with } \tau_i = \frac{Z_i \cdot e \cdot N_i^0}{\varepsilon_0} \quad \text{(S2)}$$

$$N_{i\ with\ particle}(t) = \frac{N_i^0}{1+t/\tau}, \text{ with } \tau = \frac{Z_i \cdot e \cdot (N_i^0 + qpNp)}{\varepsilon_0} \quad \text{(S3)}$$

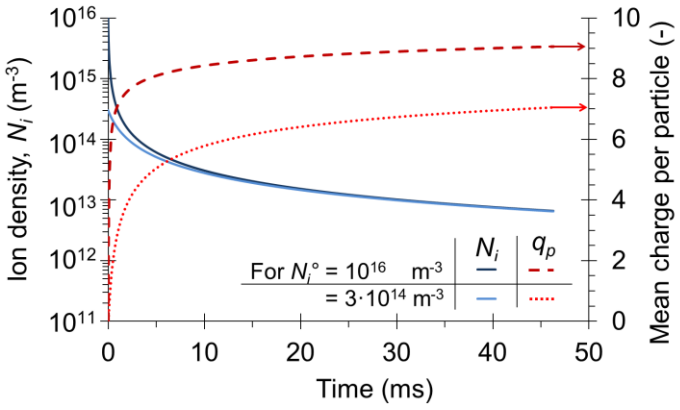

Fig. S6 Calculations of ion density and mean charge per particle q_p calculated for d_p = 350 nm with $N_i°$ of 3×10^{14} and 10^{16} m^{-3} versus time assuming constant radial ion density and aerosol concentration

In this simplified approach, for a given arrangement and transit time, a higher initial ion density leads to higher ion density in the charger. Nevertheless, due to higher space charge repulsion for the higher initial ion density, after 10 ms the ion densities differ by less than 10%. Despite the same ion density profile along the 40th last ms the final q_p reaches 7 and 9 charges for $N_i°$ of 3×10^{14} and 10^{16} m^{-3} respectively. The initial charging conditions are thus critical for the final mean charge per particle. Moreover, in a real aerosol charger, many processes have to be considered to define properly the initial charging conditions as presented below.

Fig. S7a schematically represents the trajectories of ion and particle in the charger and Fig. S7b the related ion density along particle trajectory.

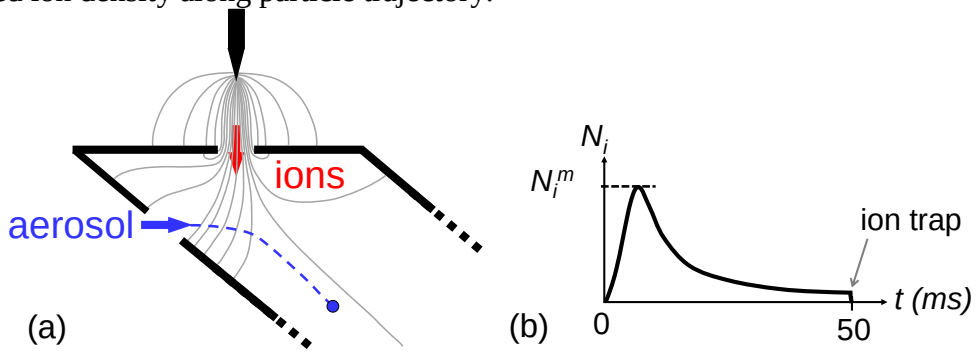

Fig. S7. Schematic representations of (a) ion and particle trajectories (b) ion density profile along a particle trajectory

After injection in the charging volume, the particles are deflected by the twice-faster ion gas velocity ($v_{aerosol} \approx 37$ m s^{-1} compared to $v_g \approx 79$ m s^{-1}) as shown in Fig. S7a, neglecting electrostatics forces on the charged particles and hydrodynamic turbulences. The temporal evolution of the ion density along particle trajectory is shown schematically in Fig. S7b. On the trajectory of any particle injected from the aerosol input in such post-discharge aerosol charger, the ion density profile increases up to a maximum value (N_i^m). Then, the particle crosses decreasing ion density up to the ion trap.

The electric field, that partly controls the ion density distribution, is the sum of three kinds of electric fields. The Laplace electric field from polarized metal electrodes, the space charge electric field (related to ion density and charged particle concentration) and the surface electric field (related to the eventual polarization of the insulator walls of the charger induced by ions losses to the walls) have to be considered. The Laplace electric field can be tuned at constant I_i^{wall} by modifying the discharge gap. For instance, for the same I_i^{wall} = 220 nA the mean charge per particle of 100 nm is 0.76 and 2 for a discharge gap of 9 mm and 5 mm. That prove that the Laplace electric field controls the ion distribution in the charging volume and thus the charging conditions. With the insulator plane, the mean charge per particle increases from 6 to 6.3 e and then decreases down to 4.5 e with increasing I_i^{wall} (cf. Table S3). The polarization of the insulator plane by the collection of ions induces a surface electric field that increases ion velocity and reduces the ion density in the charging volume.

Table S3. Influence of physical processes on the mean charge per particle versus operating conditions

Physical effect	Gap length, h(mm)	Needle voltage V_d (kV)	Discharge current I_d (µA)	I_i^{wall} (nA)	Mean particle diameter d_p (nm)	Aerosol N_p (m^{-3})	Mean charge per particle	Arrangement
Effect of aerosol concentration	4	3.8	6	31 22	600 600	8×10^{10} 1.8×10^{13}	23.3 6.3	2b (Unger, Ehouarn and Borra 2000)
Maximal ion density N_i^m	13	6.88 15	8 120	160 700	460	10^{10}	17 21	3
Laplace field	9 5	4.6 3.15	8 24	- 220	100	10^{10}	0.76 2	1 (cf. Fig 1)
Surface polarization (insulator)	5	2.82 3.27 4.27	10 30 110	130 250 710	440	7×10^{9}	6 6.3 4.5	1
Aerosol injection	10	5.4 5.5	19 15	7.5 22	440	7.9×10^{8} 3.5×10^{4}	6.4 9	2a & 2b
Aerosol injection	13	12	87	100	100	3×10^{11}	3.4 at z=2.2mm 2.1 at z=8.5mm	4

At last, the collision between ion and particle affects the ion density due to the fact that after the collision, ions are not anymore available and to the modification of the space charge (as charged particles are less mobile than ions). These are the two aspects investigated in the paper.

4.2 Particle trajectory

Due to the fast modification of particle trajectory when submitted to the perpendicular ion gas flow, the particle inertia for particle larger than 200 nm has to be taken into account in the particle trajectory and affects the maximal ion density crossed by the particle (N_i^m). Then, considering a given particle, the trajectory results from the electric and mechanical (inertia, frictional and Brownian random) forces applied on the particle. Moreover, particle trajectory depends on size and mass of the particle and on the charge evolution along its trajectory. At last, the position of particle injection affects the ion density along particle trajectory. In most cases (Huang and Alonso 2012; Unger 2001; Unger, Boulaud and Borra 2004), particle injected closer to the ion source passes through higher ion density and reach higher final mean charge than particle injected further (Cf. Table S1).

The $N_i \times \tau$ have been evaluated from data in Fig. 3 and Fuchs limiting sphere theory from 2×10^{11} to 5×10^{11} and from 5×10^{11} to 6×10^{12} $s\cdot m^{-3}$ for particle of 91 and 350 nm respectively. Despite higher post-discharge ion currents on the wall for the 9 mm gap (I_i^{wall} *= 710 nA*, for the 91 nm particle) than for the 5 mm gap (I_i^{wall} *= 580 nA* for the 350 nm particle) the $N_i \times \tau$ is lower. This is due to the polarization of the Teflon plane covering the grounded plane on the charging volume side as well as the Laplace electric field from the point that are the two main processes that affect the ion density profile in the charging volume and the related $\overline{N_i \cdot t}$ parameter. Nevertheless, these processes cannot explain the influence of aerosol concentration on the mean charge per particle presented in Fig. 4. Actually, for each particle size, the discharge operating conditions remain constant (point position, applied voltage and discharge current).

References

Alonso, M., Santos, J. P., Hontanon, E., & Ramiro, E. (2009). First Differential Mobility Analysis (DMA) Measurements of Air Ions Produced by Radioactive Source and Corona. *Aerosol and Air Quality Research, 9*(4), 453-457. doi: 10.4209/aaqr.2009.05.0033

Goldman, M., & Goldman, A. (1978). Corona discharges In M. N. Hirsh & H. J. Ascam (Eds.), *Gaseous Electronics 1, Electrical discharges* (Vol. 89b, pp. 119-166). New York: Academics Press.

Akishev, Y., O. Goossens, T. Callebaut, C. Leys, A. Napartovich, N. Trushkin. 2001. The influence of electrode geometry and gas flow on corona-to-glow and glow-to-spark threshold currents in air. *Journal of Physics D-Applied Physics* 34:2875-2882. doi: 10.1088/0022-3727/34/18/322.

Borra, J.-P., N. Jidenko, M. Alonso. 2012. Concentric electrical discharge aerosol charger: Patent WO/2014/102258, Centre national de la recherche scientifique (CNRS) (3 rue Michel Ange, Paris, Paris, F-75016, FR).

Borra, J.-P., N. Jidenko, E. Bourgeois. 2009. Atmospheric pressure plasmas for aerosols processes in materials and environment. *The European Physical Journal Applied Physics* 47:22804. doi.

Borra, J. P. 2008. Charging of aerosol and nucleation in atmospheric pressure electrical discharges. *Plasma Physics and Controlled Fusion* 28:124036. doi.

Bouarouri, A. 2014. Développement d'un chargeur à décharge couronne pour la mesure à 10 hz de la concentration d'un aérosol atmosphérique: PhD thesis of University Paris-Saclay.

Bouarouri, A., N. Jidenko, F. Gensdarmes, D. Maro, D. Boulaud, J. P. Borra. 2016. Ion current density profiles in negative corona gaps versus ehd confinements. *Journal of Electrostatics* 82:88-95. doi: http://dx.doi.org/10.1016/j.elstat.2015.08.005.

Dordizadeh, P., K. Adamiak, G. S. P. Castle. 2016. Parametric study of the characteristics of trichel pulses in the needle-plane negative corona discharge in atmospheric air. *Journal of Electrostatics* 84:73-80. doi: http://dx.doi.org/10.1016/j.elstat.2016.09.006.

Goldman, M. and A. Goldman. 1978. Corona discharges in *Gaseous electronics 1, electrical discharges* Hirsh, M. N. and H. J. Ascam, eds., 119-166. New York: Academics Press.

Goldman, M., A. Goldman, R. S. Sigmond. 1985. The corona discharge, its properties and specific uses. *Pure Appl. Chem.* 57:1353-1362. doi: 10.1351/pac198557091353.

Gopalakrishnan, R., T. Thajudeen, H. Ouyang, C. J. Hogan, Jr. 2013. The unipolar diffusion charging of arbitrary shaped aerosol particles. *Journal of Aerosol Science* 64:60-80. doi: 10.1016/j.jaerosci.2013.06.002.

Huang, C.-H. and M. Alonso. 2012. Influence of particle location on the number of charges per charged nanoparticle at the outlet of a needle charger. *Journal of the Air & Waste Management Association* 62:87-91. doi: 10.1080/10473289.2011.617609.

Jidenko, N., A. Bouarouri, F. Gensdarmes, D. Maro, D. Boulaud, J. P. Borra. 2020. Post-corona unipolar chargers with tuneable aerosol size-charge relations: Parameters affecting ion dispersion and particle trajectories for charger designs. *Aerosol Science and Technology*:1-12. doi: 10.1080/02786826.2020.1817310.

Jidenko, N., D. Maro, F. Gensdarmes, D. Boulaud, J.-P. Borra. 2012. Sub-second diffusion charging, in *European Aerosol Conference*. Grenada, Spain.

Kimoto, S., K. Saiki, M. Kanamaru, M. Adachi. 2010. A small mixing-type unipolar charger (smuc) for nanoparticles. *Aerosol Science and Technology* 44:872-880. doi: 10.1080/02786826.2010.498796.

Reischl, G. P., J. M. Mäkelä, R. Karch, J. Necid. 1996. Bipolar charging of ultrafine particles in the size range below 10 nm. *Journal of Aerosol Science* 27:931-949. doi: http://dx.doi.org/10.1016/0021-8502(96)00026-2.

Townsend, J. S. 1898. Xiii. Electrical properties of newly prepared gases. *Philosophical Magazine Series 5* 45:125-151. doi.

Trichel, G. W. 1938. The mechanism of the negative point to plane corona near onset. *Physical Review* 54:1078. doi.

Unger, L. 2001. Charge d'aérosols par décharge électrique pour la filtration d'effluents particulaires. Orsay: PhD thesis of Université Paris Sud.

Unger, L. and J.-P. Borra. 2000. Dimensionnement d ‘une décharge électrique pour l’optimisation de la charge des aérosols, in *16ème congrès Français sur les Aérosols*, pp 68-73. Paris.

Unger, L., D. Boulaud, J. P. Borra. 2004. Unipolar field charging of particles by electrical discharge: Effect of particle shape. *Journal of Aerosol Science* 35:965-979. doi.

Unger, L., P. Ehouarn, J. P. Borra. 2000. Influence of aerosol deposition on the charging efficiency of a corona charger. *Journal of Aerosol Science* 31, Supplement 1:612-613. doi.

Whitby, K. T. 1961. Generator for producing high concentrations of small ions. *Rev. Sci. Instrum.* 32:1351-1355. doi.